Applied Catalysis B: Environmental 174–175 (2015) 264–276

Contents lists available at ScienceDirect

Applied Catalysis B: Environmental

journal homepage: www.elsevier.com/locate/apcatb

Preparation of highly active unsupported nickel–zinc–molybdenum catalysts for the hydrodesulfurization of dibenzothiophene

Huan Liu, Chenguang Liu*, Changlong Yin**, Yongming Chai, Yanpeng Li, Dandan Liu, Bin Liu, Xuehui Li, Yiyan Wang, Xiuzheng Li

State Key Laboratory of Heavy Oil Processing and Key Laboratory of Catalysis of CNPC, China University of Petroleum, Qingdao 266580, PR China

ARTICLE INFO

Article history:
Received 24 October 2014
Received in revised form 7 February 2015
Accepted 10 February 2015
Available online 9 March 2015

Keywords:
Nickel–zinc–molybdenum catalyst
Hydrodesulfurization
Dibenzothiophene
Isostructural replacement
Unsupported catalyst

ABSTRACT

Nickel–zinc–molybdenum oxide catalyst precursors with various Ni/Zn molar ratios were synthesized by chemical precipitation and unsupported nickel–zinc–molybdenum sulfide catalysts were obtained by sulfidation of the precursors. The oxide precursors and unsupported sulfide catalysts were characterized by XRD, N_2 adsorption–desorption, AAS, FT-IR, TG–DSC–MS, SEM, TPR, CHSN analysis, HRTEM, and XPS. The unsupported nickel–zinc–molybdenum sulfide catalysts were tested in the hydrodesulfurization of dibenzothiophene (DBT). XRD revealed that the mesoporous nickel–zinc–molybdenum oxide precursors consisted of a phase of ammonium nickel (or zinc) molybdate. SEM showed that the Ni9.5Zn0.5Mo10 catalyst precursor contained smaller nanoparticles than the other nickel–zinc–molybdenum precursors. A reduction peak of Mo species (from Mo^{6+} to Mo^{4+}) was detected on the ternary nickel–zinc–molybdenum catalyst precursors and highly crystalline phases of MoS_2 and Ni_3S_2 nanoclusters were found on the nickel–zinc–molybdenum sulfide catalysts. XPS showed that the introduction of Zn enhanced the sulfidation of Mo species. The Ni9.5Zn0.5Mo10 catalyst showed a higher reaction rate of DBT than the other nickel–zinc–molybdenum catalysts due to the easier reduction of both oxide precursors and sulfide catalysts, and full sulfidation of Mo species, which might be attractive in industrial application.

1. Introduction

Hydrodesulfurization (HDS) has been used as the main route to remove sulfur-containing compounds from petroleum for several decades. More stringent environmental concerns for clean diesel (nowadays no more than 10–15 μg/g S) and more sulfur present in petroleum (sometimes more than 3 wt.%) brought urgent challenging problems for refineries and researchers [1]. Not only adjusting reaction conditions, but also the application of highly active HDS catalysts might be a cost-effective choice to solve this problem. HDS catalysts are traditionally composed of sulfided Mo or W, promoted by Ni or Co, and supported on a high-surface area support like alumina [1,2], but an improvement of the catalytic activity will be mandatory in the future to be able to produce clean fuel.

Highly active HDS catalysts have been prepared through several strategies, such as optimal formation of 'NiMoS' (or 'CoMoS') active phase, modification of supports, use of new supports with specific physiochemical properties, and other attempts [2–5]. Another efficient method to obtain high HDS activity is a replacement of supported HDS catalysts by unsupported or highly-loaded catalysts [6,7]. Among them, the NEBULA (new bulk activity) catalyst is a representative example. This catalyst is three times more active than the supported catalysts [6,8]. Due to its high activity, the NEBULA catalyst could produce ultra-low sulfur diesel (with less than 10 μg/g S) without having to rebuild a hydrotreating plant whose original aim was to produce diesel with 350–500 μg/g S [6].

The introduction of Zn to HDS catalysts has been reported in literature but controversial results were obtained [1,9–13]. Harris and Chianelli reported the preparation of a Zn–MoS_2 catalyst by reaction of $ZnCl_2$ with $(NH_4)_2MoS_4$ [12]. They found that Zn could not donate or withdraw any electrons from Mo since the 3d orbitals of Zn are already fully occupied, leading to little effect on the catalytic activity of MoS_2 [12]. A promoting effect of Zn in a stacked bed for spillover hydrogenation was observed by Villarroel et al., which was somewhat larger than that of Mn but not as high as that of Ni, Co, or even Fe and Cu [13]. Recently Chen et al. synthesized a series of layered NiZnMoW catalysts derived from a NiZn-layered

* Corresponding author. Tel.: +86 86981716.
** Corresponding author.
E-mail addresses: cgliu@upc.edu.cn (C. Liu), yincl@upc.edu.cn (C. Yin).

http://dx.doi.org/10.1016/j.apcatb.2015.02.009
0926-3373/

hydroxide precursor [9]. These catalysts exhibited a higher activity in the HDS of 4,6-dimethyldibenzothiophene (4,6-DMDBT) than a Zn-free NiMoW catalyst due to the difference in synergetic effect between promoter Ni/Zn and active compound Mo/W. Apparently, Zn affects the catalytic properties of MoS_2-based catalysts.

In our previous research, we synthesized a series of nickel–copper–molybdenum catalysts by chemical precipitation and prepared highly-loaded catalysts from these precursors [14]. A highly-loaded nickel–copper–molybdenum catalyst showed high activity in the HDS of 4,6-DMDBT and of fluid catalytic cracking (FCC) diesel due to the efficient formation of the 'NiMoS' active phase [14]. As a continuation of this work, a series of nickel–zinc–molybdenum oxide catalyst precursors was synthesized, and unsupported sulfide catalysts were prepared and tested in the HDS of dibenzothiophene (DBT). Various characterization techniques were employed to obtain detailed information about the physiochemical properties and HDS performance derived from the introduction of zinc.

2. Experimental

2.1. Preparation

All the reagents used were purchased from Sinopharm Chemical Reagent Company (PR China) without any further purification (Grade AR). Nickel nitrate ($Ni(NO_3)_2{\cdot}6H_2O$), zinc nitrate ($Zn(NO_3)_2{\cdot}6H_2O$), and ammonium heptamolybdate ($(NH_4)_6Mo_7O_{24}{\cdot}4H_2O$) were used for the synthesis of the NiZnMo catalyst precursors. DBT ($C_{12}H_8S$) and petroleum ether (boiling range from 90 to 120 °C) were used for catalytic reactions.

The NiZnMo catalyst precursors were synthesized through chemical precipitation, as described before [14,15]. In short, nickel nitrate (and/or zinc nitrate) and ammonium heptamolybdate were dissolved in deionized water by keeping the molar ratio (Ni + Zn)/Mo = 1 but varying the Ni/Zn ratio from 10:0, to 9.5:0.5, 8:2, 5:5, and 0:10. The solution was transferred into a flask and heated under magnetic stirring. When the temperature reached 90 °C, concentrated ammonium hydroxide (28.8% NH_3) was added dropwise to the solution, leading to the formation of a solid. Then excess of ammonium hydroxide was added to the flask, which re-dissolved the solid. At this time the pH of the solution was about 10.0. The flask was heated under mild stirring at 90 °C for 10 h. Thereafter, the solids were isolated through vacuum filtration, washed several times with deionized water, and dried for 12 h at 110 °C and atmospheric pressure. The NiZnMo catalyst precursors were named Ni_xZn_yMo10, where x and y indicate the Ni/Zn ratios mentioned above. Unsupported NiZnMo catalyst precursors were prepared by tabletting the NiZnMo precursors without any binder and then pulverizing them into 20–40 mesh size for DBT reaction.

2.2. Characterization

The NiZnMo oxide precursors and sulfided catalysts (after catalytic reaction) were characterized by a series of techniques as follows:

X-ray diffraction (XRD) characterizations were carried out at an X'Pert Pro MPD equipment produced by Panalytical with Cu Kα at a scan rate of 2° min^{-1}.

N_2 adsorption–desorption experiments were performed on a ChemBET 3000 instrument (Quantachrome, USA). Nitrogen was used as adsorption agent at −196 °C. BET surface areas were obtained from the isotherms and the total pore volumes were calculated by the BJH method. The BJH pore sizes were calculated from the desorption branch of the isotherms.

Elemental analysis was performed on a high-resolution continuum source atomic absorption spectrometer (AAS) ContrAA 700 equipment from Analytic Jena AG. Before analysis, samples were fully dissolved through hydrochloric, nitric, and sulfuric acids.

Fourier-transform infrared (FT-IR) spectra were collected from 450 to 4500 cm^{-1} on a Nexus spectrometer (Nicolet, USA) using KBr disks.

Scanning electron microscope (SEM) analysis was carried out on a FEI Quanta200 instrument.

Combined thermogravimetry, differential scanning calorimetry, and mass spectrometry analysis (TG–DSC–MS) was performed under a high-purity N_2 atmosphere at a heating rate of 10 °C min^{-1}.

Temperature-programmed reduction was carried out on a Micromeritics RS232 workstation. Before TPR experiments the samples were pre-treated by heating to 200 °C under high-purity Ar. Then the samples were cooled to room temperature and the gas was switched to 10 vol.% H_2 in Ar for 30 min at room temperature. After that, the samples were heated to the desired temperature. The consumption of H_2 was recorded by a thermal conductivity detector (TCD).

The sulfur content in the sulfided NiZnMo catalysts was analyzed by an Elementar Vario EL III elemental analyzer (CHSN analysis).

High-resolution transmission electron microscopy (HRTEM) experiments were carried out on a JEM2100 microscope operated at 200 kV.

X-ray photoelectron spectroscopy (XPS) experiment was carried out on a Thermo ESCALAB 250 spectrometer. The analytic chamber vacuum prior to testing was 5.0×10^{-9} mbar. The sulfided NiZnMo catalysts were measured by using a monochromatic Al Kα radiation (1486.6 eV) with a spot size of 500 μm. The excitation power was 15 kV × 10 mA. The elemental surface compositions of the sulfided NiZnMo catalysts were determined from the intensity of the metal (Ni 2p, Zn 2p, and Mo 3d) and sulfur peaks (S 2p) provided by the manufacturer of XPS apparatus [16]. Binding energies (BEs) were determined with C 1s (284.6 eV) as reference. A Shirley background subtraction and Gaussian (20%)–Lorentzian (80%) decomposition parameters were applied for analyzing the spectra.

2.3. Catalytic evaluation

The catalytic evaluation of the NiZnMo catalysts was carried out in a high-pressure fixed-bed stainless-steel micro reactor (10 mm i.d. and 400 mm long) operated in down-flow mode. For HDS reaction a 0.3 g portion of the unsupported NiZnMo catalyst was first diluted with quartz sand to a total volume of 2.5 cm^3, and then placed in the center of the reactor. Before catalytic reaction, the NiZnMo catalysts were in situ pre-sulfided at 330 °C for 12 h by a liquid stream containing 3.0 wt.% CS_2 dissolved in petroleum ether and H_2. After sulfidation, 1.0 wt.% DBT in petroleum ether was pumped into the reactor. The HDS reaction was carried out at a pressure of 3.0 MPa, a H_2/feed volume ratio of 400, and a weight hourly space velocity (WHSV) of 40.0 h^{-1}. To keep conversion relatively low, and thus, be able to calculate the specific reaction rates, reaction temperatures of 240 and 260 °C were selected. The HDS product was first cooled and then separated into gaseous and liquid products in a high-pressure separator behind the fixed-bed reactor. The liquid product was analyzed by a Varian 3800 gas chromatograph coupled with a quadrupole mass spectrometer (GC–MS). The GC instrument was equipped with a flame ionization detector (FID) and a 50 m OV101 capillary column.

The specific reaction rates of the NiZnMo catalysts toward DBT were calculated using the following equation [17]:

$$r_{DBT} = \frac{F}{W} \times Conv_{DBT}\,, \quad (1)$$

where r_{DBT} is the specific reaction rate of DBT (mol g^{-1} s^{-1}), F is the molar flow rate of the reactant (mol s^{-1}), w is the weight of the NiZnMo catalyst (g), and the $Conv_{DBT}$ is the conversion of DBT.

Several products were detected and confirmed by GC–MS in the HDS of DBT. Tetrahydro-dibenzothiophene (THDBT) and hexahydro-dibenzothiophene (HHDBT) are considered as hydrogenated intermediates in the hydrogenation (HYD) pathway [15] and the direct desulfurization (DDS) pathway leads to the formation of biphenyl (BP), while cyclohexylbenzene (CHB) and bicyclohexane (BCH) are the final products in the HYD pathway [15]. To estimate the selectivities of the two pathways, the following equations were employed [18]:

$$DDS = \frac{BP}{THDBT + HHDBT + BP + CHB + BCH} \times 100\% \quad (2)$$

$$HYD = \frac{THDBT + HHDBT + CHB + BCH}{THDBT + HHDBT + BP + CHB + BCH} \times 100\% \quad (3)$$

3. Results and discussion

3.1. Oxide catalyst precursor

3.1.1. XRD

The NiZnMo catalyst precursors synthesized by chemical precipitation were characterized by XRD. The XRD peaks of the NiZnMo catalysts precursors were almost identical, with peaks centered at 12.1, 17.4, 23.5, 26.5, and 29.6° (Fig. 1). For the Ni10Mo10 precursor, these peaks were ascribed to the phase of ammonium nickel molybdate ($(NH_4)HNi_2(OH)_2(MoO_4)_2$, JCPDS card no. 50-1414). This is in accordance with the Φ_y layered phases as revealed by Levin et al. [19]. In the layered structure, the tetrahedral molybdate ions are linked with the octahedral nickel, forming layers perpendicular to the *c* axis, and the ammonium ions are incorporated between the layers, compensating the electrical charge [18,19]. The XRD peaks of the Zn10Mo10 catalyst precursor were consistent with the phase of ammonium zinc molybdate. Levin et al. first reported the synthesis of ammonium zinc molybdate through the *chimie douce* method [19] and found that ammonium zinc molybdate and ammonium nickel molybdate were isostructural [20]. For the other ternary NiZnMo catalyst precursors, the similar XRD patterns indicate that the nickel (or zinc) cations can be replaced by zinc (or nickel) ions by isostructural replacement, which does not destroy the original crystal structure. We reported similar replacements of nickel by cobalt or copper in the ammonium nickel molybdate structure before [14,21], which could also maintain the original layered structure. Therefore, NiZnMo catalyst precursors with the ammonium nickel (or zinc) molybdate structure could be obtained.

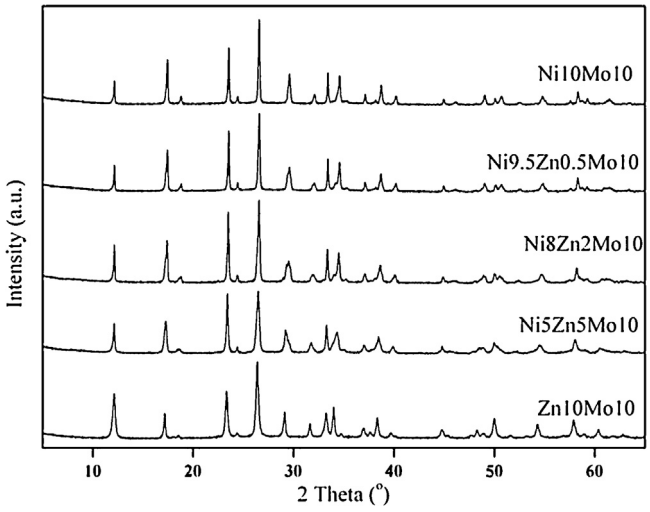

Fig. 1. XRD patterns of the NiZnMo catalyst precursors.

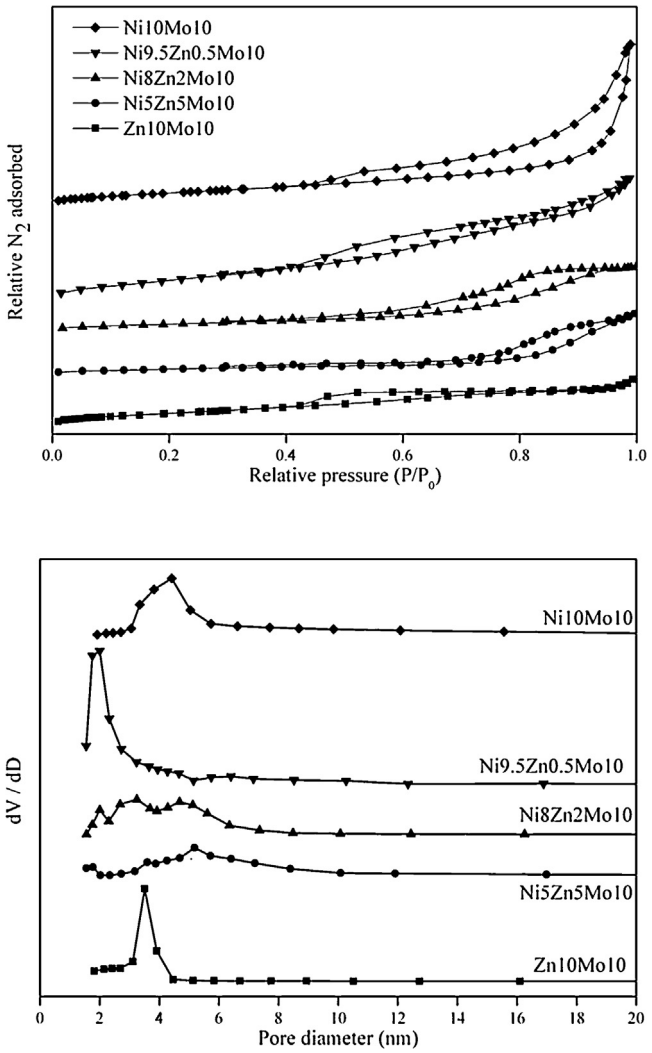

Fig. 2. N_2 isotherms and pore size distributions of the NiZnMo catalyst precursors.

3.1.2. N_2 adsorption–desorption and elemental analysis

The N_2 adsorption–desorption isotherms and pore size distributions of the NiZnMo catalyst precursors are exhibited in Fig. 2. The NiZnMo catalyst precursors exhibited type IV isotherms, which indicated that the precursors had a mesoporous structure [18,22]. According to IUPAC classification, the hysteresis loops of the isotherms of the NiZnMo catalyst precursors, except for the Ni10Mo10 precursor, were of H4-type, which might be attributed to narrow slit-like pores [22]. In our case, this pore structure might be due to the layered structure of ammonium nickel (or zinc) molybdate [19,20]. The hysteresis loop of the Ni10Mo10 precursor might be attributed to a mixture of H3- and H4-type, which is due to the formation of aggregates of plate-like particles and the layered structure [18,22], respectively. Concerning the pore size distributions of the NiZnMo catalyst precursors, the Zn10Mo10, Ni9.5Zn0.5Mo10, and Ni10Mo10 precursors showed a main peak at about 3.5, 2.0, and 4.4 nm, respectively. As for the Ni8Zn2Mo10 and Ni5Zn5Mo10 precursors, a wider pore size distribution in the range from 2 to 8 nm was confirmed.

The BET surface area, pore volume, and average pore size of the NiZnMo catalyst precursors are shown in Table 1. The BET surface areas of the binary Zn10Mo10 and Ni10Mo10 catalyst precursors

Table 1
Pore properties and elemental analysis of the NiZnMo catalyst precursors.

	S_{BET} ($m^2\ g^{-1}$)	V_P ($cm^3\ g^{-1}$)	APD (nm)	Ni[a] (at.%)	Zn[a] (at.%)	Mo[a] (at.%)	Ni:Zn:Mo
Zn10Mo10	56	0.07	4.1	–	41.4	58.6	0:1.04:1.00
Ni5Zn5Mo10	23	0.08	6.9	19.0	20.9	60.1	0.52:0.51:1.00
Ni8Zn2Mo10	35	0.09	4.8	31.4	8.2	60.4	0.85:0.20:1.00
Ni9.5Zn0.5Mo10	95	0.16	3.4	37.6	2.1	60.3	1.02:0.05:1.00
Ni10Mo10	88	0.13	4.5	39.0	–	61.0	1.05:1.00

[a] Obtained from AAS analysis.

are 56 and 88 $m^2\ g^{-1}$, respectively. For the ternary NiZnMo catalyst precursors, the BET surface areas increase with increasing Ni content. The same trend is observed for the ternary NiZnMo catalyst precursors concerning the pore volume, going from 0.08 for Ni5Zn5Mo10 to 0.16 $cm^3\ g^{-1}$ for Ni9.5Zn0.5Mo10.

Elemental analysis of the NiZnMo catalyst precursors by AAS are exhibited in Table 1. Due to chemical precipitation and isostructural replacement, Ni(Zn) was replaced by Zn(Ni) in the NiZnMo catalyst precursor, remaining the original crystal structure. These results were in accordance with the formula proposed by Levin et al. [19,20].

3.1.3. FT-IR

FT-IR characterizations were employed to gain information about the vibrations of the specific bonds. The FT-IR spectra of the NiZnMo catalyst precursors with different compositions and molar ratios are almost the same, as shown in Fig. S1. A peak at around 485 cm^{-1} is attributed to the Ni—O stretching vibration [23,24], while a FT-IR peak at about 480 cm^{-1} is due to the Zn—OH vibration [25]. These two peaks are so close that it seems very hard to be distinguished for the NiZnMo catalyst precursors. Peaks with different intensities from 1000 to 700 cm^{-1} are due to stretching vibrations of bridging Mo—O—Mo groups [26], and a peak centered at 1410 cm^{-1} is assigned to the deformation H—N—H vibration of NH_4^+ [19]. Klimova et al. found when pH is above 8, the existence of molybdenum in an aqueous solution is MoO_4^- [27], and concerning our Section 2, molybdate anion (MoO_4^-) was formed. A broad peak from 3300 to 3050 cm^{-1} is ascribed to the $\upsilon 3$ N—H asymmetric stretching vibration [19,20]. Therefore, from the FT-IR results of NiZnMo catalyst precursors it could be implied that the layered structure of the NiZnMo catalyst precursors is composed of ammonium, nickel, and zinc cations and also molybdate anions.

3.1.4. SEM

The SEM photographs of the Zn10Mo10, Ni5Zn5Mo10, Ni8Zn2Mo10 and Ni9.5Zn0.5Mo catalyst precursors (Fig. 3) show that the Zn10Mo10 catalyst precursor consists of disorderly stacked thick plates. The Ni5Zn5Mo10 catalyst precursor contains smaller plates compared but with the same morphology. The Ni8Zn2Mo10 catalyst precursor forms larger three-dimensional structures but the plate structure could also be detected. The morphology of the Ni9.5Zn0.5Mo10 catalyst precursor is different from those of the other NiZnMo precursors. Some dense but small nanoparticles of about 50 nm diameter are formed, covering the larger particles. Our formed works showed that the Ni10Mo10 precursor contains disorderly stacked particles with size from 200 to 1000 nm [14].

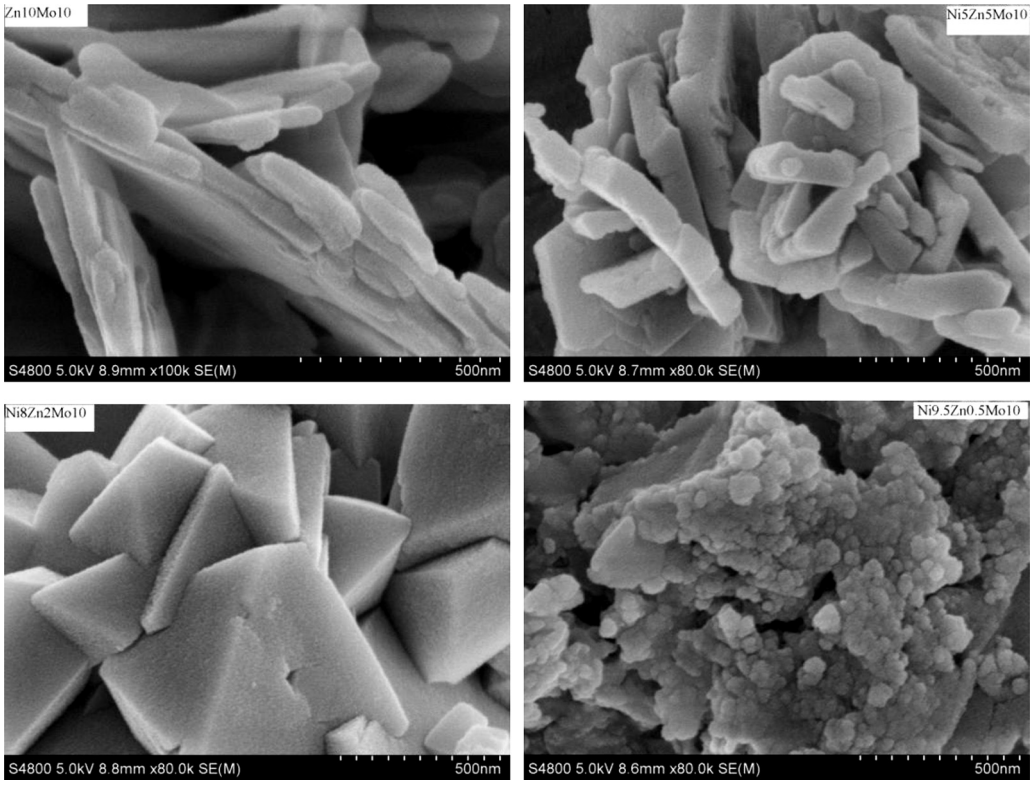

Fig. 3. SEM micrographs of the NiZnMo catalyst precursors.

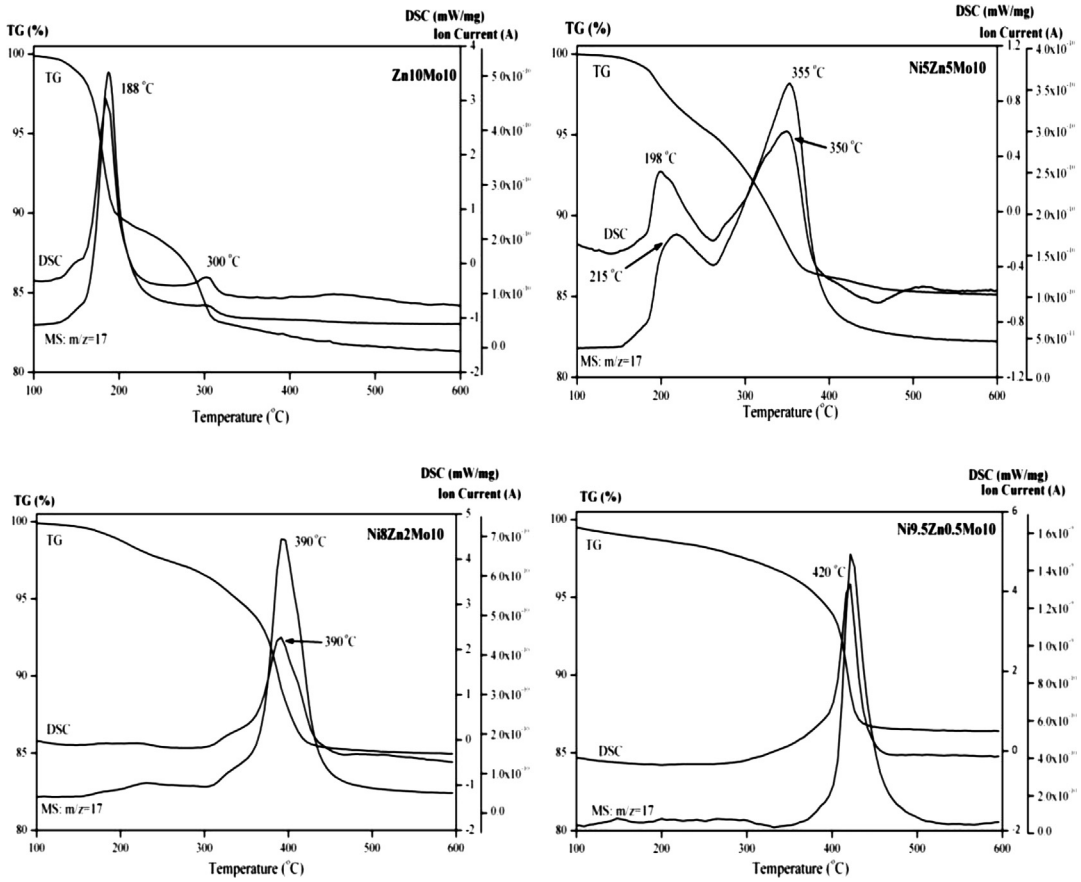

Fig. 4. TG–DSC–MS curves of the NiZnMo catalyst precursors.

3.1.5. TG–DSC–MS

The TG–DSC–MS curves of the Ni10Mo10 catalyst precursor exhibit an endothermic peak at 407 °C, as reported previously [7]. The endothermic TG peak is accompanied by a weight loss of 11.0% between 350 and 500 °C, and MS reveals that H_2O and NH_3 are released in this region. The weight loss of the Zn10Mo10 catalyst precursor from 140 to 305 °C could be divided into two continuous steps (Fig. 4). The first step is from 140 to 195 °C with a weight loss of 8.6%, and the release of H_2O (m/z = 18, not shown here) and NH_3 (m/z = 17) as detected by the MS curve, followed by a weight loss peak from 195 to 305 °C (weight loss 6.7%). The DSC curve shows a strong endothermic peak at 188 °C and a relatively weak endothermic peak at 300 °C, which are attributed to the decomposition and dehydration of the Zn10Mo10 catalyst precursor [28,29]. The TG–DSC–MS curves of the Ni5Zn5Mo10 catalyst precursor exhibit a two-step decomposition. From 150 to 265 °C an endothermic DSC peak occurs at 198 °C and a peak related to the release of H_2O and NH_3 (MS curve) occurs at 215 °C. The weight loss in this temperature region is 4.9%, while a subsequent weight loss from 265 to 410 °C is 8.7%. MS confirms the release of NH_3 and H_2O. The curves of the Ni8Zn2Mo10 and Ni9.5Zn0.5Mo10 catalyst precursors are very similar and also similar to that of the Ni10Mo10 precursor [7]. The Ni8Zn2Mo10 and Ni9.5Zn0.5Mo10 catalyst precursors have a strong endothermic peak at 390 and 420 °C, respectively. The weight loss of the Ni8Zn2Mo10 catalyst precursor from 285 to 460 °C is 11.6% and the Ni9.5Zn0.5Mo10 catalyst precursor shows a weight loss of 9.4% from 360 to 460 °C. The endothermic peaks and the decomposition of these two precursors are accompanied by the release of H_2O and NH_3, as revealed by the MS results (Fig. 4).

3.1.6. TPR

The reductive abilities of the NiZnMo catalyst precursors were studied by H_2-TPR and the results are depicted in Fig. 5. The Ni10Mo10 catalyst precursor exhibits a main reduction peak from 400 to 600 °C, which is due to the reduction of Mo species [2,11,14]. The Zn10Mo10 catalyst precursor shows a TPR peak attributed to the reduction of Mo-containing compound from 560 to 685 °C.

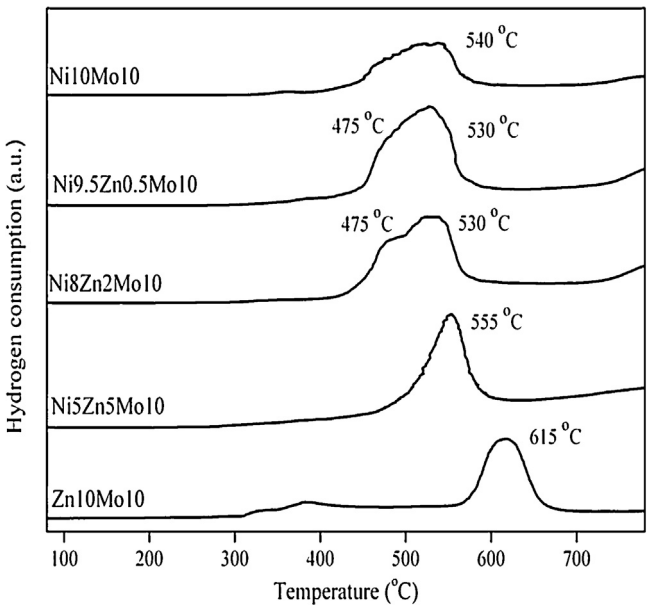

Fig. 5. TPR patterns of the NiZnMo catalyst precursors.

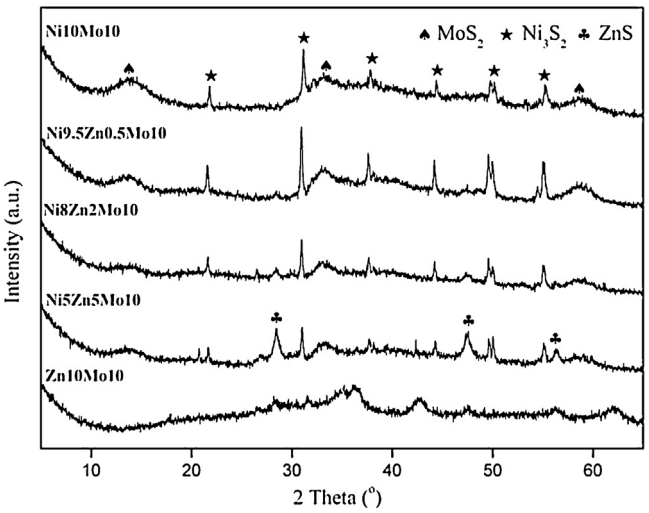

Fig. 6. XRD patterns of the sulfided NiZnMo catalysts.

The reduction peaks related to Mo species of the ternary NiZnMo catalyst precursors are centered at various temperatures. The Ni5Zn5Mo10 catalyst precursor exhibits a H_2 consumption peak from 465 to 610 °C related to the reduction of Mo species, while the reduction of Mo species (from 420 to 585 °C) for the Ni8Zn2Mo10 and Ni9.5Zn0.5Mo10 catalyst precursors could be divided into two steps. According to literature [11,30], the former reduction peak centered at 475 °C is due to the reduction of Mo^{6+} in octahedral sites to Mo^{4+}, and the later peak at 530 °C is ascribed to the reduction of Mo species in tetrahedral sites, which are more difficult to reduce.

These assignments show that with increasing content of zinc in the NiZnMo catalyst precursors, the main reduction peaks attributed to the Mo species are shifted to higher temperature (from 475 and 530 °C for the Ni9.5Zn0.5Mo10 catalyst precursor to 615 °C for the Zn10Mo10 catalyst precursor). Chen et al. found that the addition of Zn to a NiMoW catalyst promoted the reducibility of Ni species but retarded the reducibility of Mo or W species [9], which is in agreement with our results. The reduction peaks at 475 °C for the Ni9.5Zn0.5Mo10 and Ni8Zn2Mo10 catalyst precursors are due to the Mo^{6+} species in octahedral sites [11,30]. Linares and Fernández found that the introduction of Zn to NiMo/γ-Al_2O_3 catalyst would increase Mo species in octahedral sites, which showed a higher activity toward DBT [11]. Besides, the temperature regions for the reduction of the Ni9.5Zn0.5Mo10 and Ni8Zn2Mo10 catalyst precursors are consistent with that of the Ni10Mo10 catalyst precursor, but the relative H_2 consumptions of these precursors are higher than that of the Ni10Mo10 precursor.

3.2. Sulfided NiZnMo catalysts

3.2.1. XRD

A highly amorphous phase attributed to MoS_2 with XRD peaks at 2θ = 14, 33, 38 and 58° was detected for all sulfided Ni-containing NiZnMo catalysts (Fig. 6), but not for the Zn10Mo10 catalyst [7,18]. XRD peaks due to Ni_3S_2 (JCPDS card No. 44-1418) were observed at 2θ about 22, 31, 38, 44, 50, and 55° [7,14]. Compared to the broad peaks of the MoS_2 phase, the sharp Ni_3S_2 peaks attributed to the Ni_3S_2 phase had higher intensity in the Ni10Mo10, Ni9.5Zn0.5Mo10, and Ni8Zn2Mo10 catalysts, indicating the high crystallinity of the Ni_3S_2 phase [18]. XRD peaks in the Ni5Zn5Mo10 catalyst at 2θ about 29, 47, and 56° are due to the ZnS phase (JCPDS card no. 01-0792) [31]. These peaks could hardly be observed for the Ni8Zn2Mo10 and Ni9.5Zn0.5Mo10 catalysts, implying a high dispersion of the sulfided zinc species in these two catalysts. Due to the poor crystallinity of the Zn10Mo10 catalyst, no phases were observed in our present work.

The characteristic (0 0 2) peak of the MoS_2 phase (2θ at 14°) is better visible for the Ni10Mo10 and Ni9.5Zn0.5Mo10 catalysts than for the other NiZnMo catalysts, indicating the formation of more agglomerated MoS_2 nanoparticles. The Ni_3S_2 phase shows a similar trend. Altamirano et al. proposed the simultaneous formation of Ni_3S_2 and MoS_2, which might be due to the decomposition of the 'NiMoS' active phase ($NiMoS \rightarrow Ni_3S_2 + MoS_2$) [32]. In that case, the detection of Ni_3S_2 and MoS_2 phases for the NiZnMo catalysts might be beneficial for HDS reactions.

3.2.2. N_2 adsorption–desorption and elemental analysis

The pore properties of the sulfided NiZnMo catalysts are exhibited in Table 2 and their N_2 adsorption–desorption isotherms and pore size distributions are in Fig. 7. The sulfided NiZnMo catalysts were analyzed by AAS and CHSN analysis and results are also reported in Table 2. After HDS reaction, the BET surface areas of the NiZnMo catalysts decreased, while little changes about atomic ratios were observed of the sulfided NiZnMo catalysts. The BET surface area of the ternary NiZnMo catalyst decreased from 5.7 to 10.2 $m^2\,g^{-1}$ and its pore volume decreased from 0.02 to 0.03 $cm^3\,g^{-1}$. Compared with the data of the NiZnMo oxide catalyst precursors (Table 1), larger average pore size together with smaller BET surface area and pore volume of the NiZnMo sulfide catalysts were formed after HDS reaction. This might be partially due to lack of support and the formation of agglomerated sulfides. From Table 2 it could be found that the sulfur content of the sulfided Zn10Mo10 catalyst was only 11.8%, which was much lower those of the other NiZnMo catalysts (32.2–33.2%), indicating the incomplete sulfidation of the Zn10Mo10 catalyst.

Fig. 7 shows that the mesoporous structure of the sulfided NiZnMo catalysts is remarkable (type IV) and the hysteresis loops of the isotherms of the sulfided NiZnMo catalysts are of H4-type, consistent with those of the NiZnMo catalyst precursors (Fig. 2) [22]. This implies that after HDS reaction the layered structure of the NiZnMo catalyst precursors could be retained. Li and co-workers proposed that a layered structure is beneficial for a better dispersion of active species, and thus, leads to high HDS activity [9,33]. Fig. 7 also depicts the pore size distributions of the sulfided NiZnMo catalysts. Different from the results in Fig. 2, all the sulfided NiZnMo catalysts showed a main peak from 3.5 to 4.0 nm.

Table 2
Pore properties and elemental analysis of the sulfided NiZnMo catalyst.

	S_{BET} ($m^2\,g^{-1}$)	V_P ($cm^3\,g^{-1}$)	APD (nm)	Ni[a] (at.%)	Zn[a] (at.%)	Mo[a] (at.%)	S[b] (wt.%)	Ni:Zn:Mo:S
Zn10Mo10	19.7	0.01	8.1	–	45.0	55.0	11.8	0:1.20:1.00:0.73
Ni5Zn5Mo10	5.7	0.02	12.2	19.0	21.2	59.8	33.2	0.52:0.52:1.00:2.49
Ni8Zn2Mo10	10.0	0.03	9.5	31.3	9.4	59.3	32.7	0.86:0.23:1.00:2.45
Ni9.5Zn0.5Mo10	10.2	0.03	9.0	37.9	2.3	59.8	32.2	1.04:0.06:1.00:2.38
Ni10Mo10	14.3	0.03	6.8	40.4	–	59.6	33.2	1.11:0:1.00:2.49

[a] Obtained from AAS analysis.
[b] Obtained from CHSN analysis.

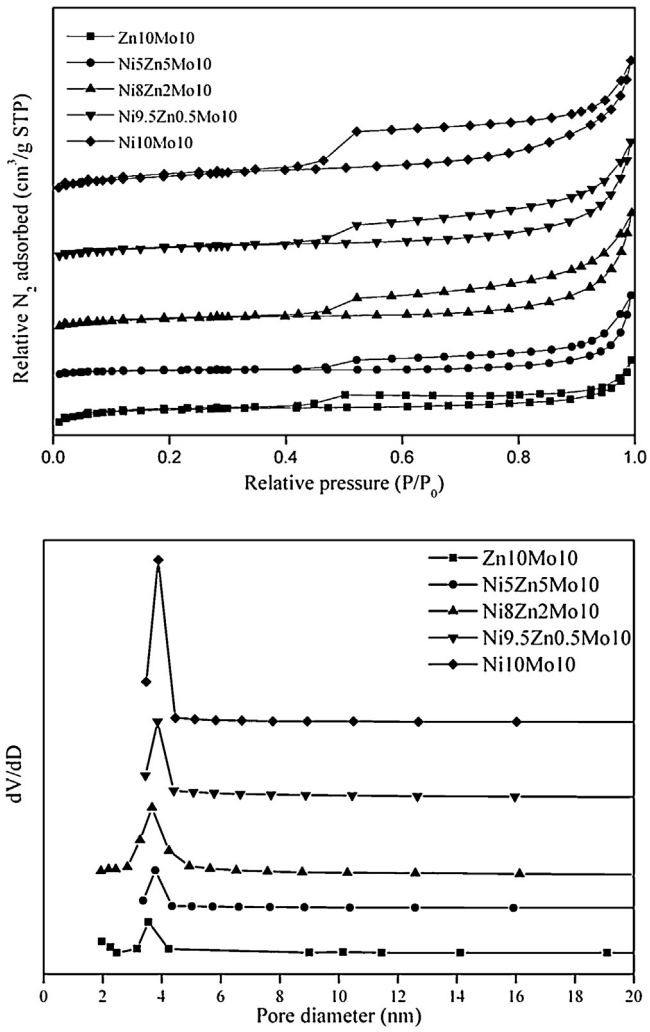

Fig. 7. N_2 Isotherms and pore size distributions of the sulfided NiZnMo catalysts.

3.2.3. HTREM micrographs

The sulfided NiZnMo catalysts were characterized by HTREM to obtain more detailed information about the dispersion of active compounds and typical HTREM micrographs are presented in Fig. S2. The characteristic black MoS_2 layers, whose inter-planar distance of the typical (0 0 2) basal planes is about 0.62 nm, were observed for all sulfided NiZnMo catalysts [2,7,33]. The stacking numbers of the MoS_2 layers of the Zn10Mo10 catalyst were lower than those of the other NiZnMo catalysts. This is in agreement with the XRD results of the sulfided NiZnMo catalysts. The MoS_2 slabs over the Ni9.5Zn0.5Mo10 catalyst are highly disorderedly stacked, and it was difficult to calculate the average stacking number and slab length. Characteristic layers corresponding to sulfided Zn or Ni species were not detected [7,31], implying that the sulfided Zn or Ni species are highly dispersed in the sulfided NiZnMo catalysts.

3.2.4. TPR

The sulfided NiZnMo catalysts were characterized by H_2-TPR (Fig. 8). The TPR pattern of the sulfided Ni10Mo10 catalyst has been published before [14]. The H_2 consumption peak at about 275 °C is ascribed to the reduction of sulfided nickel species located at the edges of MoS_2 nanoparticles forming the 'NiMoS' active phase and the peak at 443 °C is ascribed to the MoS_2 nanoparticles [14,34]. In the TPR pattern of the sulfided Zn10Mo10 catalyst a small H_2 consumption peak appeared centered at about 210 °C, which might be due to the H_2S generated by the hydrogenation of the nonstoichiometric sulfur (S_x) from the catalyst surface [28,34,35]. A relatively intense H_2 uptake peak started at 515 °C and did not end until 700 °C. Due to limitations of our instrument, we cannot collect data at higher temperature. This H_2 uptake peak centered at 665 °C for the Zn10Mo10 catalyst is attributed to the reduction of bulk MoS_2 nanoclusters [34]. In accordance with these results, no H_2 uptake peak due to the reduction of ZnS was observed, because the reduction of ZnS is much less favorable than that of MoS_2 nanoparticles [31]. Various types of H_2 consumption peaks were observed for the ternary NiZnMo catalysts. The Ni5Zn5Mo10 catalyst exhibited two H_2 consumption peaks at 208 and 617 °C, similar to the Zn10Mo10 catalyst. These two peaks might be attributed to the hydrogenation of the nonstoichiometric sulfur (S_x) and the reduction of the bulk MoS_2 nanoclusters. However, the reduction peak due to bulk MoS_2 nanoclusters shifted to lower temperature from 665 °C for the Zn10Mo10 catalyst to 617 °C for the Ni5Zn5Mo10 catalyst, which indicates that the introduction of nickel is beneficial for the reduction of Mo species. The beneficial effect is more remarkable for the Ni8Zn2Mo10 and Ni9.5Zn0.5Mo10 catalysts. The reduction peaks assigned to bulk MoS_2 nanoclusters decreased to 450 and 442 °C for the Ni8Zn2Mo10 and Ni9.5Zn0.5Mo10 catalysts, respectively, similar to the reduction temperature of Mo species over the Ni10Mo10 catalyst. A similar trend has also been observed by Nielsen et al. [36]. They found that the introduction of Ni or Co to MoS_2-based catalysts led to a lower temperature position of TPR peak as compared to non-promoted MoS_2 catalyst, which implied a decreasing metal–sulfur bond energy [36].

3.2.5. XPS

XPS spectra were collected and decomposed using as iterative least squares computer program XPSPEAK version 4.1 as described elsewhere [37]. The Mo 3d XPS spectra of the sulfided NiZnMo catalysts are depicted in Fig. 9 and the corresponding parameters are reported in Table 3. As reported [5,30,34,37], for sulfided MoS_2-based HDS catalysts, several Mo species with various valencies might exist and these species could be easily distinguished through the differences of BEs. Molybdenum disulfide (MoS_2) appears at 228.7 ± 0.2 eV (Mo^{IV} $3d_{5/2}$), and molybdenum oxide (MoO_3) is located at 232.6 ± 0.2 eV (Mo^{VI} $3d_{5/2}$), while another molybdenum oxysulfide species (MoO_xS_y) is approximately at 230.6 ± 0.2 eV (Mo^{V} $3d_{5/2}$) [5,30,34,37]. From Fig. 8, these Mo-based species were detected in the sulfided NiZnMo catalysts. The Zn10Mo10 catalyst exhibited XPS peaks attributed to MoS_2, MoO_3, and MoO_xS_y species. As for other NiZnMo catalysts, no peak due to MoO_3 specie was detected. The Ni8Zn2Mo10 and Ni10Mo10 catalysts showed XPS peaks attributed to MoS_2 and MoO_xS_y species. The Ni9.5Zn0.5Mo10

Table 3
XPS parameters of Mo 3d and S 2s and atomic ratios of the sulfided NiZnMo catalysts.

	Mo^{IV}		Mo^{V}		Mo^{VI}		S	Ni:Zn:Mo:S
	BE (eV)	(at.%)	BE (eV)	(at.%)	BE (eV)	(at.%)	BE (eV)	
Zn10Mo10	228.8	10	230.1	67	232.1	23	226.0	0:1.2:1.0:1.3
Ni8Zn2Mo10	228.5	74	229.5	26	–	0	225.9	0.7:0.3:1.0:3.7
Ni9.5Zn0.5Mo10	228.7	100	–	0	–	0	225.8	0.8:0.1:1.0:3.6
Ni10Mo10	228.6	69	230.1	31	–	0	225.9	0.7:0:1.0:2.6

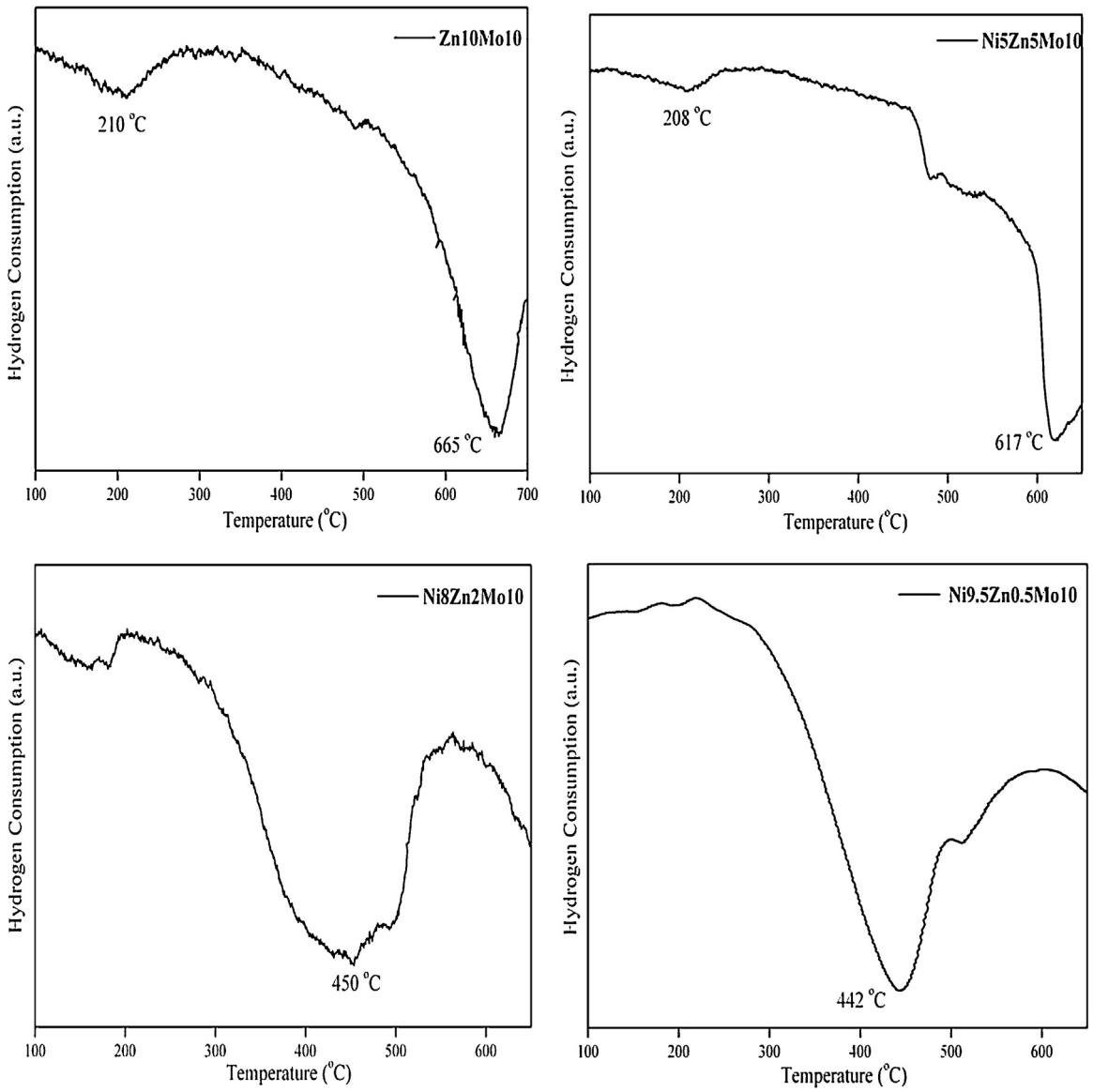

Fig. 8. TPR patterns of the sulfided NiZnMo catalysts.

catalyst showed a peak due to MoS_2, implying full sulfidation of Mo species of this catalyst. Besides, a broad peak centered at about 226.0 eV is attributed to the S 2s line and was subtracted from the total spectra of Mo 3d [5,37]. From Table 3, the fraction of MoS_2 (Mo^{IV}) of the Ni10Mo10 catalyst was 69%, which was a little lower than that of the Ni8Zn2Mo10 catalyst (74%), and the fraction of MoS_2 (Mo^{IV}) of the Ni9.5Zn0.5Mo10 catalyst was 100%. This implies that the introduction of Zn to NiMo-based catalysts enhances the sulfidation of Mo species.

The Ni 2p XPS spectra of the sulfided NiZnMo catalysts were analyzed and shown in Fig. 10. As for the sulfided Ni10Mo10 catalyst, an XPS peak at 852.3 ± 0.2 eV was attributed to metallic Ni specie [38,39], which might be formed due to high content of Ni. XPS peaks centered at 853.0 ± 0.2 and 853.7 ± 0.2 eV were ascribed to sulfided Ni species (i.e., Ni_3S_2, NiS, or Ni_9S_8) and Ni in 'NiMoS' active phase, respectively [34,37]. Besides, an XPS peak located at 856.1 ± 0.2 eV was due to Ni oxide species [37]. As for the ternary NiZnMo catalysts, XPS peaks were confirmed at 855.1 ± 0.2 eV on the Ni8Zn2Mo10 and Ni9.5Zn0.5Mo10 catalysts. Yang et al. reported that the binding energy of Ni $2p_{3/2}$ decreased to about 855.1 eV with increasing content of ZnO to supported Ni catalysts, which was due to the improved inter-phase interaction between ZnO and Ni species on the surface [40]. At the same time, a XPS peak at 852.5 ± 0.2 was detected over these ternary NiZnMo catalysts and could also be attributed to metallic Ni [41,42]. The atomic ratios on the catalyst surfaces are obtained by XPS and reported in Table 3. Combined the data from AAS and CHSN (in Table 2) and from XPS (in Table 3) analysis, it could be found that the content of nickel in the bulk was a little higher than that on the surface, while the content of zinc showed a reverse tread over the ternary NiZnMo catalysts. This is in accordance with the results reported by Yang et al. [40]. Besides, higher contents of sulfur on the surface were observed than in the bulk over the NiZnMo catalysts.

3.3. HDS results

DBT was used to study the HDS reaction over the NiZnMo catalysts. This molecule is typically used as model for sulfur-containing

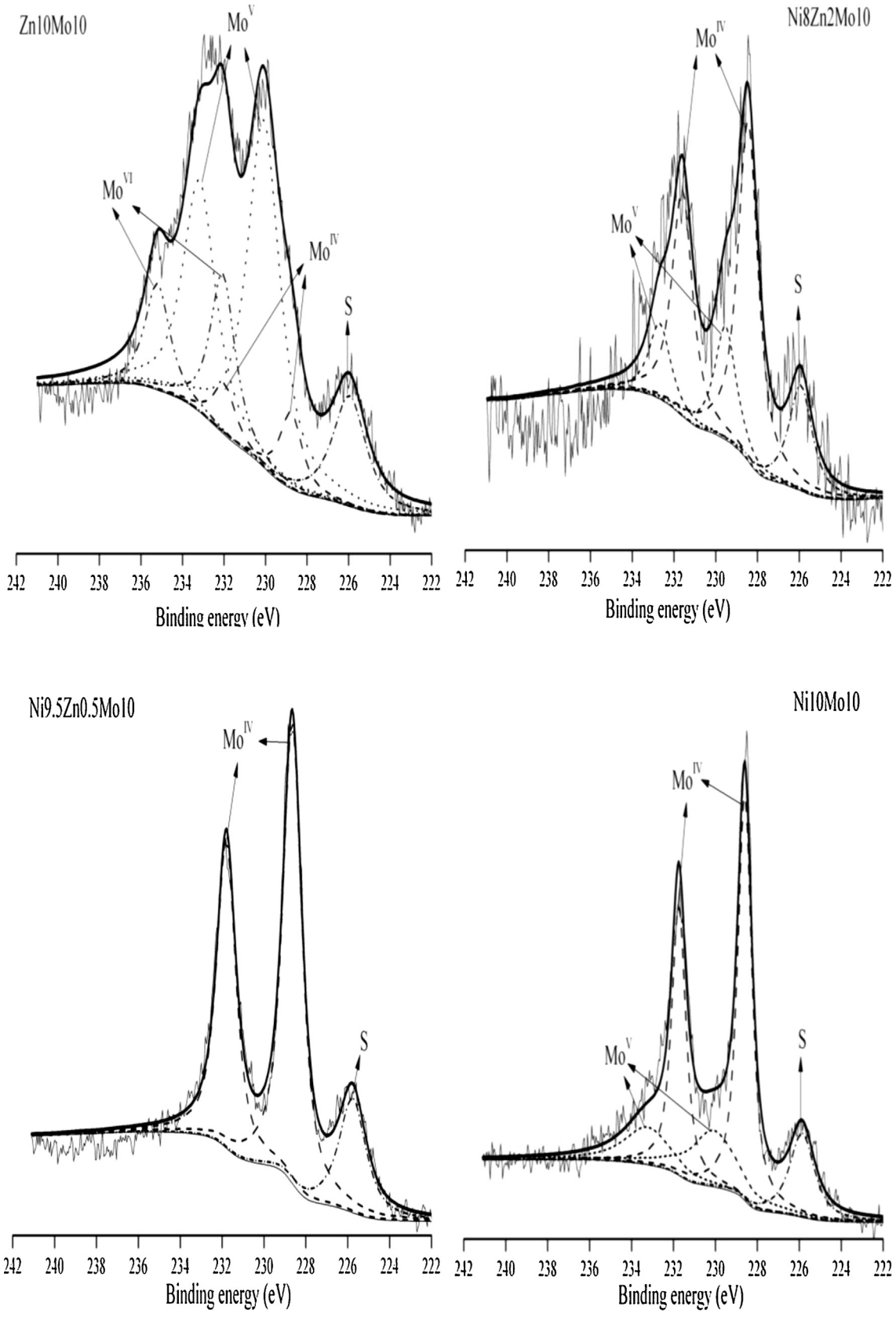

Fig. 9. Mo 3d XPS spectra of the sulfided NiZnMo catalysts.

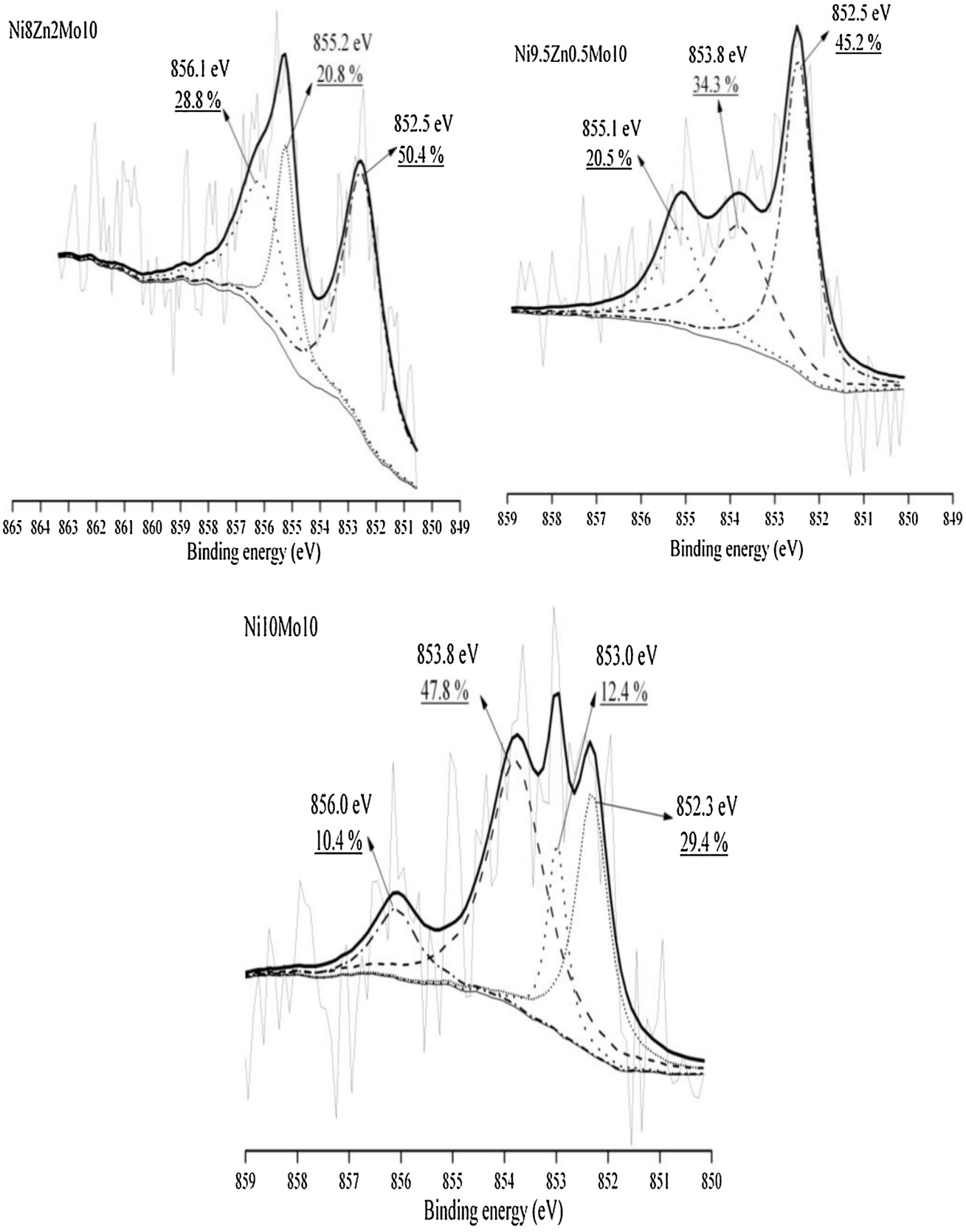

Fig. 10. Ni 2p XPS spectra of the sulfided NiZnMo catalysts.

Table 4
Catalytic results of the sulfided NiZnMo catalyst reacted at 240 °C.

Catalyst	Conversion (%)	TH-DBT	HH-DBT	BP	CHB	BCH	Rate (10^{-9} × mol g^{-1} s^{-1})	HYD/DDS
Zn10Mo10	1.2	0	16.7	16.7	66.6	0	7	5.0
Ni5Zn5Mo10	3.5	15.8	5.3	21.1	52.6	5.2	21	3.7
Ni8Zn2Mo10	5.2	21.6	3.9	25.5	41.2	7.8	31	2.9
Ni9.5Zn0.5Mo10	10.9	19.3	5.5	30.3	44.9	0	66	2.3
Ni10Mo10	10.0	22.8	6.9	30.7	39.6	0	60	2.2

compounds in petroleum [2]. The HDS mechanism of DBT over MoS_2-based catalysts has been widely reported in literature and two distinct pathways have been distinguished [15,43,44]. One pathway is called direct desulfurization (DDS), which involves the cleavage of the C—S bonds of DBT through hydrogenolysis, and leads to the formation of BP. The other pathway is hydrogenation (HYD). In this pathway, first an aromatic ring of DBT is hydrogenated and intermediates, including THDBT and HHDBT, are formed. Then scission of the C—S bonds takes place, which yields CHB and BCH. Recently Valencia et al. proposed the detailed DDS and HYD mechanisms and the Gibbs energy profiles of DBT-like compounds based on the density functional theory (DFT) calculations [45]. The results of the HDS reactions over the NiZnMo catalysts at 240 and 260 °C are exhibited in Tables 4 and 5, respectively. With increasing temperature (from 240 to 260 °C), the HDS reaction rates of the NiZnMo catalysts increased remarkably. As expected, poor activity was observed for the Zn10Mo10 catalyst, while the Ni9.5Zn0.5Mo10 catalyst had the highest HDS activity. The introduction of zinc to MoS_2-based catalysts could not substantially improve the HDS activity, as Ni or Co promoters do [11,17]. As mentioned before, the lack of synergy is attributed to the electronic effect of Zn, which is not involved in the formation of Zn—Mo—S bonds due to the low energy of the 3d orbitals of zinc, and therefore does not affect MoS_2 electronically [12]. The poor activity of the Zn10Mo10 catalyst could also be related to the higher reduction temperature of the oxide precursor (Fig. 5), which needs a higher temperature for sulfidation [18], thus, inhibits the HDS reactions. This is confirmed by the TPR results of the sulfided NiZnMo catalysts (Fig. 8). The reduction temperature of MoS_2 nanoclusters over the Zn10Mo10 catalyst was higher than over the other catalysts, which means that the reduction of the Zn10Mo10 sulfide catalyst is difficult. At the same time, TG–DSC–MS results revealed that the Zn10Mo10 catalyst precursor decomposed at lower temperature (188 °C) than the other NiZnMo precursors, which would be more easily sintered, and thus, lead to a poor catalytic performance [46].

The ratio of the HYD and DDS pathways of the NiZnMo catalysts was calculated according to Eqs. (2) and (3) and is shown in Tables 4 and 5. Due to increasing reaction temperature, the HYD/DDS ratio of the NiZnMo catalysts decreased except for the Zn10Mo10 catalyst. The Zn10Mo10 catalyst showed a higher HYD/DDS ratio than the other NiZnMo catalysts, and reached 12.0 at 260 °C. At this temperature, the HYD/DDS ratio for the Ni10Mo10 and Ni9.5Zn0.5Mo10 catalysts was 1.8, which is the smallest HYD/DDS ratio observed in this work. The results reveal that during the HDS reaction of DBT the HYD pathway plays a predominant role, especially at lower temperature. According to the HDS mechanism of DBT raised by Valencia et al. [45], HYD pathway was more favorable than DDS pathway because HYD pathway possessed lower energetic barriers than DDS pathway. At the same time, thermodynamics of HDS reactions might also provide some rational explanation. The HDS reactions of organic sulfur-containing compounds are exothermic, while reactions of sulfur-containing compounds to yield unsaturated hydrocarbons and H_2S are endothermic. Therefore, at increasing reaction temperature, the DDS pathway becomes more favorable relative to the HYD pathway [47].

The product distributions over the NiZnMo catalysts at 240 and 260 °C are also shown in Tables 4 and 5, respectively. Several products, including THDBT, HHDBT, BP, CHB, and BCH, were detected by GC–MS. CHB was the abundant product over the Zn10Mo10 catalyst. Especially at 260 °C, the selectivity of CHB was more than 80%. Meanwhile, the HYD/DDS ratio reached 12.0 (Table 4). To some extent, the preference of the HYD pathway for the Zn10Mo10 catalyst is similar to that for the non-promoted MoS_2 based catalysts. This is in accordance with the results reported by Egorova and Prins [43]. They studied a non-promoted Mo/γ-Al_2O_3 catalyst and Ni and Co-promoted Mo/γ-Al_2O_3 catalysts, and found that the Mo/γ-Al_2O_3 catalyst mainly catalyzed the HYD pathway, and that the content of BP was much smaller than for the Co or Ni-promoted Mo/γ-Al_2O_3 catalysts [43].

The high selectivity of CHB for the Zn10Mo10 catalyst is due to the dispersion of the active compounds, and can be interpreted by the 'Rim-Edge' model. According to the 'Rim-Edge' model proposed by Daage and co-workers aiming at correlating the catalytic properties with the specific sites [48,49], the HDS results indicates that the Zn10Mo10 catalyst possesses more Rim reaction sites [48,49]. The refractory molecule DBT could easily absorb onto these sites and undergo the following catalytic reactions. This is in accordance with the characterization results of the sulfided Zn10Mo10 catalysts. As discussed before, HRTEM micrographs (Fig. S2) showed that the Zn10Mo10 catalyst exhibited smaller slab length and a lower number of stacked MoS_2 nanoparticles than the other NiZnMo catalysts. Fig. 6 exhibited that the typical XRD peak attributed to the MoS_2 phase could not be detected for the Zn10Mo10 catalyst. The XRD and HRTEM results were in accordance with the XPS results, which revealed that the fraction of MoS_2 (Mo^{IV}) was only 10%, indicating the uncompleted sulfidation of this catalyst. The difficult sulfidation of Zn was also revealed by CHSN analysis as shown in Table 2 with the sulfur content of 11.8 wt.%. TPR pattern (Fig. 8) indicated that the sulfided Zn10Mo10 catalyst needed a high temperature for reduction, which implied the intense interaction between metal and sulfur. This might be

Table 5
Catalytic results of the sulfided NiZnMo catalyst reacted at 260 °C.

Catalyst	Conversion (%)	TH-DBT	HH-DBT	BP	CHB	BCH	Rate (10^{-9} × mol g^{-1} s^{-1})	HYD/DDS
Zn10Mo10	3.9	0	10.3	7.6	82.1	0	24	12.0
Ni5Zn5Mo10	6.3	16.3	6.2	24.5	46.9	6.1	38	3.1
Ni8Zn2Mo10	10.4	11.8	5.9	30.4	37.3	14.6	63	2.3
Ni9.5Zn0.5Mo10	22.1	10.6	3.2	35.5	50.7	0	133	1.8
Ni10Mo10	15.5	13.1	4.6	35.3	43.8	3.2	94	1.8

detrimental for the formation of active phase for HDS reactions [36].

The Ni9.5Zn0.5Mo10 catalyst showed a higher HDS activity than the other NiZnMo catalysts, reaching 66 and 133 × 10^{-9} mol g^{-1} s^{-1} at 240 and 260 °C, respectively. However, the Ni 2p XPS results (Fig. 10) showed that the fraction of 'NiMoS' active phase on the Ni9.5Zn0.5Mo10 catalyst (34.3%) was lower than that on the Ni10Mo10 catalyst (47.8%), and no XPS peak attributed to 'NiMoS' active phase could be observed on the Ni8Zn2Mo10 catalyst. On the other hand, no Ni oxide species were detected over the Ni9.5Zn0.5Mo10 catalyst. Therefore, based on the catalytic performances and the XPS results, we might infer that less nickel in oxide species would lead to higher HDS activity. The reaction rate of the Ni9.5Zn0.5Mo10 catalyst is about 1.4 times higher than that of the Ni10Mo10 catalyst at 260 °C. Similar results were observed by Chen et al. [9]. They found for the NiZnMoW catalysts that when the molar Ni:Zn ratio reached 8.6, the highest activity in the HDS of 4,6-DMDBT was obtained, which was about 1.7 times higher than for the Zn-free NiMoW catalyst. The high catalytic activity of the Ni9.5Zn0.5Mo10 catalyst might be related to some specific physicochemical properties. Compared to other NiZnMo catalysts, smaller nanoparticles were formed on the Ni9.5Zn0.5Mo10 precursor as revealed by the SEM results. The TPR results (Fig. 5) showed that the reduction of the Mo species occurred in two steps. The TPR peak at 475 °C was due to the reduction of the Mo species in octahedral site, and the increased Mo species in octahedral site was beneficial for HDS reactions as reported by Linares et al. [11]. XRD results of the sulfided Ni9.5Zn0.5Mo10 catalyst showed typical phases of MoS_2 and Ni_3S_2 with high intensity compared to the other catalysts, and disorderly stacked MoS_2 slabs were observed by HRTEM. XPS results showed that the fraction of MoS_2 (Mo^{IV}) of the Ni9.5Zn0.5Mo10 catalyst was 100%. The sulfided Ni9.5Zn0.5Mo10 catalyst exhibited a lower H_2-reduction temperature of MoS_2 nanoparticles than the other catalysts. This indicated that the weaker interaction between metal and sulfur was confirmed in the Ni9.5Zn0.5Mo10 catalyst, which might enhance the catalytic activity [36]. Therefore, the easier reduction of the Ni9.5Zn0.5Mo10 catalyst precursor from Mo^{6+} to Mo^{4+} might account for its high catalytic activity. Our previous work and relevant results show that calcination temperatures and activation temperatures play fundamental roles in preparing highly-active HDS catalysts [15,18], so, further focus would be paid on these vital factors to enhance the catalytic activity of the Ni9.5Zn0.5Mo10 catalyst.

4. Conclusions

Homogeneous NiZnMo oxide catalyst precursors were synthesized by chemical precipitation. XRD results revealed that nickel (or zinc) could be substituted by zinc (or nickel) in the NiZnMo oxide catalyst precursors due to isostructural replacement, leading to the formation of ammonium nickel (or zinc) molybdate. The variation of composition and molar ratio of the NiZnMo oxide catalyst precursors led to various decomposition and reduction temperatures, pore properties and morphologies. Sulfided NiZnMo catalysts exhibited the typical XRD peaks of MoS_2 and the Ni_3S_2 and ZnS phases could be detected on the Ni5Zn5Mo10 catalyst. The reduction of Mo^{6+} to Mo^{4+} was observed on the Ni9.5Zn0.5Mo10 catalyst precursor and the reduction peak of MoS_2 nanoparticles decreased from 665 °C on the Zn10Mo10 catalyst to 442 °C on the Ni9.5Zn0.5Mo10 catalyst. XPS results revealed that the fraction of MoS_2 (Mo^{IV}) were enhanced by introduction of Zn, and that of the Ni9.5Zn0.5Mo10 catalyst was 100%. The results of the HDS of DBT showed that the Zn10Mo10 catalyst had a poor catalytic activity and a high HYD selectivity to CHB (more than 80% at 260 °C), while the Ni9.5Zn0.5Mo10 catalyst had a higher reaction rate than the other catalysts. The Ni9.5Zn0.5Mo10 catalyst with lower reduction temperature of Mo^{6+} to Mo^{4+} in the oxide state and MoS_2 in the sulfide state, and full sulfidation of Mo species, showed higher catalytic activity, which might deserve industrial application in the future.

Acknowledgements

This work was financially supported by the National Natural Science Fund of China (grant nos. U1162203 and 21106185) and the Fundamental Research Funds for the Central Universities (grant nos. 14CX06032A and 14CX02059A). Financial support from PetroChina Corporation Limited is also greatly appreciated.

Appendix A. Supplementary data

Supplementary data associated with this article can be found, in the online version, at http://dx.doi.org/10.1016/j.apcatb.2015.02.009.

References

[1] T.C. Ho, Catal. Today 98 (2004) 3–18.
[2] L. Peña, D. Valencia, T. Klimova, Appl. Catal. B: Environ. 147 (2014) 879–887.
[3] J. Lauritsen, J. Kibsgaard, G. Olesen, P. Moses, B. Hinnemann, S. Helveg, J. Nørskov, B. Clausen, H. Topsøe, E. Lægsgaard, F. Besenbacher, J. Catal. 249 (2007) 220–233.
[4] A.S. Walton, J.V. Lauritsen, H. Topsøe, F. Besenbacher, J. Catal. 308 (2013) 306–318.
[5] P.A. Nikulshin, D.I. Ishutenko, A.A. Mozhaev, K.I. Maslakov, A.A. Pimerzin, J. Catal. 312 (2014) 152–169.
[6] F.L. Plantenga, R. Cerfontain, S. Eijsbouts, F. van Houtert, G.H. Anderson, S. Miseo, S. Soled, K. Riley, K. Fujita, Y. Inoue, Sci. Technol. Catal. 89 (2002) 407–410.
[7] C. Yin, L. Zhao, Z. Bai, H. Liu, Y. Liu, C. Liu, Fuel 107 (2013) 873–878.
[8] R.R. Chianelli, G. Berhault, B. Torres, Catal. Today 147 (2009) 275–286.
[9] Y. Chen, L. Wang, Y. Zhang, T. Liu, X. Liu, Z. Jiang, C. Li, Appl. Catal. A: Gen. 474 (2014) 69–77.
[10] C.F. Linares, J. López, A. Scaffidi, C.E. Scott, Appl. Catal. A: Gen. 292 (2005) 113–117.
[11] C.F. Linares, M. Fernández, Catal. Lett. 126 (2008) 341–345.
[12] S. Harris, R.R. Chianelli, J. Catal. 98 (1986) 17–31.
[13] M. Villarroel, P. Baeza, N. Escalona, J. Ojeda, B. Delmon, F.J. Gil-Llambías, Appl. Catal. A: Gen. 345 (2008) 152–157.
[14] H. Liu, C. Yin, H. Li, B. Liu, X. Li, Y. Chai, Y. Li, C. Liu, Fuel 129 (2014) 138–146.
[15] H. Liu, C. Yin, B. Liu, X. Li, Y. Li, Y. Chai, C. Liu, Energy Fuel 28 (2014) 2429–2436.
[16] J.A. Toledo-Antonio, M.A. Cortés-Jácome, C. Angeles-Chávez, J. Escobar, M.C. Barrera, E. López-Salinas, Appl. Catal. B: Environ. 90 (2009) 213–223.
[17] D. Genuit, P. Afanasiev, M. Vrinat, J. Catal. 235 (2005) 302–317.
[18] S.L. Amaya, G. Alonso-Núñez, T.A. Zepeda, S. Fuentes, A. Echavarría, Appl. Catal. B: Environ. 148–149 (2014) 221–230.
[19] D. Levin, S.L. Soled, J.Y. Ying, Inorg. Chem. 35 (1996) 4191–4197.
[20] D. Levin, S.L. Soled, J.Y. Ying, Chem. Mater. 8 (1996) 836–843.
[21] C. Yin, H. Liu, X. Li, Y. Wang, B. Liu, L. Zhao, C. Liu, Catal. Lett. 144 (2014) 285–292.
[22] K.S.W. Sing, D.H. Everett, R.A.W. Haul, L. Moscou, R.A. Pierotti, J. Rouquérol, T. Siemieniewska, Pure Appl. Chem. 57 (1985) 603–619.
[23] G. Duan, W. Cai, Y. Luo, F. Sun, Adv. Funct. Mater. 17 (2007) 644–650.
[24] H. Zhang, H. Liu, X. Cao, S. Li, C. Sun, Mater. Chem. Phys. 79 (2003) 37–42.
[25] J.T. Kloprogge, L. Hickey, R.L. Frost, J. Solid State Chem. 177 (2004) 4047–4057.
[26] W.M. Shaheen, Mater. Lett. 52 (2002) 272–282.
[27] T.E. Klimova, D. Valencia, J.A. Mendoza-Nieto, P. Hernández-Hipólito, J. Catal. 304 (2013) 29–46.
[28] G. Zhang, S. Yu, Y. Yang, W. Jiang, S. Zhang, B. Huang, J. Cryst. Growth 312 (2010) 1866–1874.
[29] C. Peng, L. Gao, S. Yang, J. Sun, Chem. Commun. 43 (2008) 5601–5603.
[30] R. Nava, R.A. Ortege, G. Alonso, C. Ornelas, B. Pawelec, J.L.G. Fierr, Catal. Today 127 (2007) 70–84.
[31] E. Blanco, D. Uzio, G. Berhault, P. Afanasiev, J. Mater. Chem. A 2 (2014) 3325.
[32] E. Altamirano, J. Delosreyes, F. Murrieta, M. Vrinat, J. Catal. 235 (2005) 403–412.
[33] L. Wang, Y. Zhang, Y. Zhang, P. Liu, H. Han, M. Yang, Z. Jiang, C. Li, Appl. Catal. A: Gen. 394 (2011) 18–24.
[34] E. Rodríguez-Castellón, A. Jiménez-López, D. Eliche-Quesada, Fuel 87 (2008) 1195–1206.

[35] E. Puello-Polo, A. Gutiérrez-Alejandre, G. González, J.L. Brito, Catal. Lett. 135 (2010) 212–218.
[36] L.P. Nielsen, S.V. Christensen, H. Topsøe, B.S. Chausen, Catal. Lett. 67 (2000) 81–85.
[37] W. Lai, W. Song, L. Pang, Z. Wu, N. Zheng, J. Li, J. Zheng, X. Yi, W. Fang, J. Catal. 303 (2013) 80–91.
[38] X. Li, W. Zhang, Langmuir 22 (2006) 4638–4642.
[39] J. Juan-Juan, M.C. Román-Martínez, M.J. Illán-Gómez, Appl. Catal. A: Gen. 355 (2009) 27–32.
[40] L. Yang, Z. Jiang, G. Fan, F. Li, Catal. Sci. Technol. 4 (2014) 1123–1131.
[41] J.C. Jesus, I. González, A. Quevedo, T. Puerta, J. Mol. Catal. A: Chem. 228 (2005) 283–291.
[42] S. Velu, K. Suzuki, M. Vijayaraj, S. Barman, C.S. Gopinath, Appl. Catal. B: Environ. 55 (2005) 287–299.
[43] M. Egorova, R. Prins, J. Catal. 225 (2004) 417–427.
[44] H. Wang, R. Prins, J. Catal. 264 (2009) 31–43.
[45] D. Valencia, L. Peña, I. Garía-Cruz, Int. J. Quantum Chem. 112 (2012) 3599–3605.
[46] L. Medici, R. Prins, J. Catal. 163 (1996) 38–49.
[47] S.A. Ali, Pet. Sci. Technol. 25 (2007) 841–852.
[48] M. Daage, R.R. Chianelli, J. Catal. 149 (1994) 414–427.
[49] A. Wang, Y. Wang, T. Kabe, Y. Chen, A. Ishihara, W. Qian, J. Catal. 199 (2001) 19–29.